J. Fluid Mech. (2014), *vol.* 753, *pp.* 104–130.
doi:10.1017/jfm.2014.325

Test of the anomalous scaling of passive temperature fluctuations in turbulent Rayleigh–Bénard convection with spatial inhomogeneity

Xiaozhou He[1,‡], Xiao-dong Shang[2] and Penger Tong[1,†]

[1]Department of Physics, Hong Kong University of Science and Technology, Clear Water Bay, Kowloon, Hong Kong

[2]State Key Laboratory of Tropical Oceanography, South China Sea Institute of Oceanology, Chinese Academy of Sciences, Guangzhou 510301, China

(Received 22 March 2013; revised 2 June 2014; accepted 5 June 2014)

The scaling properties of the temperature structure function (SF) and temperature–velocity cross-structure function (CSF) are investigated in turbulent Rayleigh–Bénard convection (RBC). The measured SFs and CSFs exhibit good scaling in space and time and the resulting SF and CSF exponents are obtained both at the centre of the convection cell and near the sidewall. A universal relationship between the CSF exponent and the thermal dissipation exponent is found, confirming that the anomalous scaling of passive temperature fluctuations in turbulent RBC is indeed caused by the spatial intermittency of the thermal dissipation field. It is also found that the difference in the functional form of the measured SF and CSF exponents at the two different locations in the cell is caused by the change of the geometry of the most dissipative structures in the (inhomogeneous) temperature field from being sheetlike at the cell centre to filament-like near the sidewall. The experiment thus provides direct evidence showing that the universality features of turbulent cascade are linked to the degree of anisotropy and inhomogeneity of turbulent statistics.

Key words: Rayleigh–Bénard convection, intermittency, turbulent flows

1. Introduction

Fluid turbulence is often considered as a cascade process in which kinetic energy is being transferred from large to small scales (Kolmogorov 1941; Frisch 1995). To characterize the cascade process, one considers the longitudinal velocity structure function (SF), $S_u^n(r) = \langle |u(x+r) - u(x)|^n \rangle_{x,t} = \langle \delta u_r^n \rangle$, of the velocity increment δu_r between two points separated by a distance r along the flow direction. Kolmogorov's refined similarity hypothesis predicted that (Kolmogorov 1962)

$$S_u^n(r) \sim \langle \epsilon_u(r)^{n/3} \rangle r^{n/3} \sim r^{\zeta_u(n)}, \tag{1.1}$$

† Email address for correspondence: penger@ust.hk

‡ Present address: Max Planck Institute for Dynamics and Self Organization, D-37073 Göttingen, Germany

where the energy dissipation rate $\epsilon_u(r) = \langle \epsilon_u \rangle_r$ averaged over a spherical volume of radius r is scale-dependent because of the spatial intermittency of the viscous dissipation field. Such a non-space-filling dissipation field gives rise to the anomalous scaling exponents $\zeta_u(n)$ (Frisch 1995).

Similar problems of anomalous scaling also apply to a scalar field advected by a turbulent velocity field, such as temperature fluctuations $T(x, t)$ in turbulent thermal convection. In this case, one considers the temperature SF, $S_T^n(r) = \langle |T(x+r) - T(x)|^n \rangle_{x,t} = \langle \delta T_r^n \rangle$, of the temperature increment δT_r between two points separated by a distance r. When the temperature is a passive scalar, one has (Obukhov 1949; Corrsin 1951)

$$S_T^n(r) \sim \langle \epsilon_u(r)^{-n/6} \epsilon_T(r)^{n/2} \rangle r^{n/3} \sim r^{\zeta_T(n)}, \tag{1.2}$$

where the volume-averaged thermal dissipation rate $\epsilon_T(r) = \langle \epsilon_T \rangle_r$ also becomes scale-dependent because of the spatial intermittency of the thermal dissipation field.

The intermittency problem of passive scalars has been studied and understood in the Kraichnan model (Kraichnan 1974, 1994), in which Kraichnan derived an analytical expression for the reduced exponent $\zeta_T(n)/\zeta_T(2)$. The 'linear ansatz' used in the Kraichnan model was later called into question (Frisch, Mazzino & Vergassola 1998; Falkovich, Gawedzki & Vergassola 2001) and Kraichnan's prediction of $\zeta_T(n)/\zeta_T(2)$ was also known not to fit the available data (Warhaft 2000). In the past decades, there has been a large number of theoretical (Procaccia & Zeitak 1989, 1990; She & Orszag 1991; Sreenivasan 1991*b*; Grossmann & Lohse 1992; Benzi *et al.* 1993; Grossmann & Lohse 1993; She & Léveque 1994; Chertkov *et al.* 1995; Gawędzki & Kupiainen 1995; Shraiman & Siggia 1995; Cao & Chen 1997; Shraiman & Siggia 2000; Ching & Chau 2001; Ching 2007; Arnèodo *et al.* 2008), numerical (Cao, Chen & Sreenvasan 1996; Kerr 1996; Calzavarini, Toschi & Tripiccione 2002; Camussi & Verzicco 2004; Ching, Guo & Lo 2008), and experimental (Wu *et al.* 1990; Procaccia *et al.* 1991; Tong & Shen 1992; Benzi *et al.* 1994; Cioni, Ciliberto & Sommeria 1995; Takeshita *et al.* 1996; Ashkenazi & Steinberg 1999; Zhou & Xia 2001; Skrbek *et al.* 2002; Mashiko *et al.* 2004) studies of small-scale velocity and temperature fluctuations in turbulent flows. Details about these studies have been reviewed by Sreenivasan (1991*a*), Siggia (1994), Warhaft (2000), Biferale & Procaccia (2005), Ishihara, Gotoh & Kaneda (2009), Lohse & Xia (2010) and Chilla & Schumacher (2012). Many experimental studies focused on the velocity and temperature SFs, aimed at testing the anomalous scaling. Figure 1 summarizes the main experimental results obtained in locally homogeneous turbulent flows, such as grid turbulence (Gylfason & Warhaft 2004; Lepore & Mydlarski 2009) and heated jet (Antonia *et al.* 1984) and wake (Meneveau *et al.* 1990; Ruiz-Chavarria, Baudet & Ciliberto 1996). Experiments were also carried out in turbulent Rayleigh–Bénard convection (RBC), where a thin layer of fluid is heated from below and cooled from the top (Siggia 1994; Kadanoff 2001; Lohse & Xia 2010). Recently, the space-resolved velocity and temperature SFs were obtained in turbulent RBC at the cell centre and near the sidewall (Sun, Zhou & Xia 2006; Kunnen *et al.* 2008). The convective flow in a small-aspect-ratio cell is spatially inhomogeneous and has different characteristics at these two locations (Qiu & Tong 2001; Xi, Lam & Xia 2004). While some of the early data show some scatterers, the entire body of data shown in figure 1 clearly reveal two distinct behaviours beyond the experimental uncertainties, with turbulent RBC near the sidewall belonging to one group and the rest of the data sets being the other group. These two different behaviours clearly demonstrate the effect of spatial

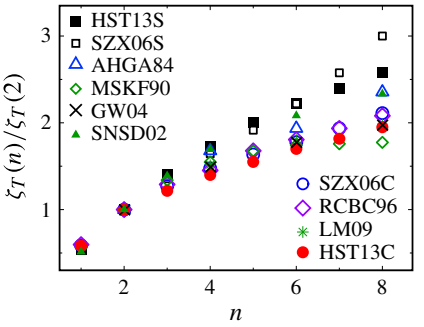

FIGURE 1. (Colour online) Reduced scaling exponent $\zeta_T(n)/\zeta_T(2)$ as a function of n obtained in various experiments: HST13S (black solid squares, present work, RBC near the sidewall); SZX06S (black open squares, Sun *et al.* (2006), RBC near the sidewall); AHGA84 (triangles (blue online), Antonia *et al.* (1984), heated jet); MSKF90 (diamonds (green online), Meneveau *et al.* (1990), heated wake); GW04 (black crosses, Gylfason & Warhaft (2004), grid turbulence); SZX06C (circles (blue online), Sun *et al.* (2006), RBC at the cell centre); RCBC96 (diamonds (purple online), Ruiz-Chavarria *et al.* (1996), heated wake); LM09 (flakes (green online), Lepore & Mydlarski (2009), grid turbulence); HST13C (solid circles (red online), present work, RBC at the cell centre).

inhomogeneity of turbulence on the temperature SFs. How to incorporate the spatial inhomogeneity effect into the intermittency of passive scalars is an interesting and open question and certainly deserve a further study.

Furthermore, to test the refined similarity ideas for anomalous scaling, one not only needs to check the scaling properties of the velocity and temperature SFs, but also should examine the scale-dependent statistics of the dissipation fields, in order to verify that the observed anomalous scaling is indeed compatible with the scaling of the dissipation fields. In contrast to the large number of experimental studies of the velocity and temperature SFs, direct measurements of the viscous and thermal dissipation rates in turbulent flows are rare (Warhaft 2000; Lohse & Xia 2010). This is partially due to the fact that simultaneous measurements of all of the components of the velocity gradient tensor or the temperature gradient vector with adequate spatial and temporal resolutions are still challenging tasks.

More recently, we made a local temperature gradient probe consisting of four identical thermistors and used it to measure the instantaneous thermal dissipation rate, $\epsilon_T(\boldsymbol{x}, t) = \kappa|\nabla T(\boldsymbol{x}, t)|^2$, in turbulent RBC (He, Tong & Xia 2007; He & Tong 2009). Here κ is the thermal diffusivity and $\nabla T(\boldsymbol{x}, t)$ is the temperature gradient field. From the single-point time series measurements, we constructed a locally averaged thermal dissipation rate (He, Tong & Ching 2010*b*; He *et al.* 2011),

$$\epsilon_T(\tau) = \frac{1}{\tau}\int_t^{t+\tau} \epsilon_T(\boldsymbol{x}, t')\,\mathrm{d}t', \tag{1.3}$$

and studied the τ-dependence of the moments, $\langle[\epsilon_T(\tau)]^n\rangle$. Both at the cell centre and near the sidewall, the measured $\langle[\epsilon_T(\tau)]^n\rangle$ exhibit good scaling in τ, i.e.

$$\langle[\epsilon_T(\tau)]^n\rangle \sim \tau^{\mu(n)}, \tag{1.4}$$

for all values of n up to six. The obtained values of $\mu(n)$ (for integers of n) are given in table 1. The experiment provided a solid foundation for a further study of

	Sidewall					Centre				
n	ζ_T^*	$\zeta_{Tu}(n)$	$\mu(n)$	$\theta(-n/3, n)$	$\phi(n, 2n)$	ζ_T^*	$\zeta_{Tu}(n)$	$\mu(n)$	$\theta(-n/3, n)$	$\phi(n, 2n)$
0.5	0.55	0.56 ± 0.01	0.053	0.013	−0.008	0.58	0.65 ± 0.01	0.062	0.036	-0.028 ± 0.01
1	1	1	0	0.046	−0.026	1	1	0	0.11	-0.092 ± 0.02
1.5	1.40	1.38 ± 0.01	−0.089	0.092	−0.047	1.22	1.26 ± 0.02	−0.16	0.19	-0.15 ± 0.04
2	1.73	1.73 ± 0.03	−0.22	0.15	−0.064	1.40	1.53 ± 0.05	−0.37	0.28	-0.18 ± 0.05
2.5	2.00	2.05 ± 0.05	−0.39	0.20	−0.071	1.55	1.84 ± 0.07	−0.63	0.36	-0.17 ± 0.07
3	2.22	2.34 ± 0.07	−0.59	0.26	−0.066	1.70			0.43	
3.5	2.40	2.63 ± 0.09	−0.82	0.32	−0.051	1.82			0.50	
4	2.58	2.89 ± 0.11	−1.06	0.38	−0.029	1.95			0.57	

TABLE 1. Summary of the obtained scaling exponents near the sidewall (first five columns) and at the cell centre (last five columns). Here $\zeta_T^* = \zeta_T(2n)/\zeta_T(2)$ and the values of $\mu(n)$ for integers of n are obtained from He, Ching & Tong (2011).

the relationship between the scaling properties of the temperature SFs and thermal dissipation field.

In this paper, we report a systematic investigation of the scaling properties of the temperature SF $S_T^n(r)$ and temperature–velocity cross-structure functions (CSFs) $S_{Tu}^n(\tau)$ in turbulent RBC. The measured $S_T^n(r)$ and $S_{Tu}^n(\tau)$ are found to exhibit good scaling in space r and time τ and the resulting exponents $\zeta_T(n)$ and $\zeta_{Tu}(n)$ are obtained at the centre of the convection cell and near the sidewall; at both locations the local temperature fluctuations behave like a passive scalar (more discussions are given in § 3 below). A universal relationship between the CSF exponent $\zeta_{Tu}(n)$ and the thermal dissipation exponent $\mu(n)$ is found, confirming that the anomalous scaling of passive temperature fluctuations in turbulent RBC is indeed caused by the spatial intermittency of the thermal dissipation field. The experiment also demonstrates that the difference in the functional form of the measured $\zeta_T(n)$ and $\zeta_{Tu}(n)$ at the two different locations in the cell is caused by the change of the geometry of the most dissipative structures in the (inhomogeneous) temperature field from being sheetlike at the cell centre to filament-like near the sidewall.

2. Experiment

All of the convection experiments were conducted in a upright cylindrical cell filled with water. The inner diameter of the cell is $D = 19.0$ cm and its height $H = 20.5$ cm. The corresponding aspect ratio of the cell is $\Gamma = D/H \simeq 1$. The sidewall of the cell is made of a transparent Plexiglas ring, which is sandwiched between the top cooling plate and bottom heating plate. The entire cell is placed inside a thermostat box, whose temperature matches the mean temperature of the bulk fluid and is maintained at $40 \pm 0.3\,^{\circ}\mathrm{C}$. More details about the apparatus and experimental method have been described elsewhere (He & Tong 2009). The control parameter of the convection experiments is the Rayleigh number Ra, which is defined as $Ra = \alpha g \Delta T H^3/(\nu\kappa)$, where g is the gravitational acceleration, ΔT is the temperature difference across the fluid layer and α, ν and κ are, respectively, the thermal expansion coefficient, the kinematic viscosity and the thermal diffusivity of the fluid. In the experiment, Ra is varied in the range $9 \times 10^8 \leqslant Ra \leqslant 2 \times 10^{10}$ and the Prandtl number, $Pr = \nu/\kappa$, is fixed at $Pr \simeq 4.3$.

Two types of experimental data are used in the analysis to be described below. The first type of data were obtained from simultaneous two-point temperature measurements, which were made using two movable thermistors of 0.2 mm in diameter and 15 ms in time constant at a sampling rate of 40 Hz. For the measurements in the sidewall region, one of the thermistors was fixed at the middle height of the cell and 2 cm away from the sidewall. The other thermistor was placed above the fixed one with a varying vertical separation r along the downstream direction of the large-scale circulation. The value of r was varied in the range 0–16 mm with the resolution of 1 μm. For the measurements in the central region of the cell, one of the thermistors was fixed at the cell centre and the other (movable) thermistor was put aside from the fixed one with a varying horizontal separation r along the cell diameter. The horizontal separation r was varied in the range 0–90 mm with the same resolution of 1 μm. More details about the measurements have been reported previously (He *et al.* 2010*b*, 2011). From the two-point time series measurements, we calculate the temperature SF, $S_T^n(r) = \langle \delta T_r^n \rangle$, of the temperature increment δT_r with varying r. For each value of r, we collected over 10-h-long time series data (1.4×10^6 data points), which ensures an adequate convergence level for a

temperature SF of order up to 8. Great care is taken to analyse the scaling property of $S_T^n(r)$ and obtain the scaling exponent $\zeta_T(n)$ in (1.2).

The second type of data were obtained from the simultaneous measurements of the local temperature $T(t)$ and vertical velocity $u_z(t)$, which is the longitudinal velocity component near the sidewall. The velocity measurement was conducted using a laser Doppler velocimetry (LDV) system together with an argon-ion laser. The mean sampling rate of the velocity measurements was ∼42 Hz near the cell sidewall and ∼20 Hz at the cell centre. For each respective location, we took 33- and 14-h-long time series data. They correspond to $\sim 5 \times 10^6$ and $\sim 10^6$ data points, respectively, ensuring that the statistical average of the flow properties is adequate. Simultaneous velocity and temperature measurements were carried out using a multichannel LDV interface module to synchronize the data acquisition. A triggering pulse from the LDV signal processor initiates the acquisition of an analogue temperature signal. A small movable thermistor of 0.2 mm in diameter, 15 ms in time constant and 1 mK Ω^{-1} in temperature sensitivity was used to measure $T(t)$ at a location very close to the LDV laser focusing spot. In the experiment, the spatial separation between the LDV focusing spot and the thermistor tip was kept at a minimal value of 0.7 ± 0.2 mm. The LDV focusing spot was always placed at an upstream position to further minimize the disturbance of the thermistor to the velocity measurement. This body of data has been used previously to study the spatial distribution and scaling property of the local convective heat flux (Shang *et al.* 2003, 2004; Shang, Tong & Xia 2008).

From the single-point time series measurements of $T(t)$ and $u_z(t)$, we calculate the temperature–velocity CSF (Boratav & Pelz 1998),

$$S_{Tu}^n(\tau) = \langle \delta u_\tau^n \delta T_\tau^{2n} \rangle_t \sim \tau^{\zeta_{Tu}(n)}, \tag{2.1}$$

with the temperature increment $\delta T_\tau = |T(t+\tau) - T(t)|$ and velocity increment $\delta u_\tau = |u_z(t+\tau) - u_z(t)|$. Note that the temperature–velocity CSF S_{Tu}^n, as defined in (2.1), requires the power index ratio between δu_τ and δT_τ to be 1:2. As will be shown below (see (3.1)), the scaling property of S_{Tu}^n defined above is uniquely linked to that of the thermal dissipation rate ϵ_T. In the above, we have assumed $S_{Tu}^n(\tau) \sim \tau^{\zeta_{Tu}(n)}$ and the validity of this assumption will be checked below. We will study the dependence of the CSF on delay time τ for different values of n.

3. Results and discussion

It has been shown (Qiu & Tong 2001; Sun, Xia & Tong 2005) that the velocity field in a closed convection cell is neither homogeneous nor isotropic. In the central region, the mean flow is zero and velocity fluctuations are approximately homogeneous. The velocity field near the sidewall is anisotropic with a dominant mean flow in the vertical direction. The spatial inhomogeneity and anisotropy are caused by the non-uniform distribution of the thermal plumes in the cell. The recent temperature (Qiu & Tong 2002), velocity (Qiu & Tong 2001; Sun *et al.* 2005), local heat flux (Shang *et al.* 2004) and flow visualization (Xi *et al.* 2004) measurements have revealed that the thermal plumes in a closed cylindrical cell organize themselves in such a way that warm plumes accumulate on one side of the cell and cold plumes concentrate on the opposite side of the cell. This plume distribution is clearly shown in figure 2, which is a flow visualization image of small thermochromic liquid crystal (TLC) spheres seeded in the convecting fluid (water). These TLC spheres change colour from red to blue over a temperature range of 4 °C (29–33 °C). In the flow visualization, a thin (2 mm in thickness) vertical sheet of white light was shone

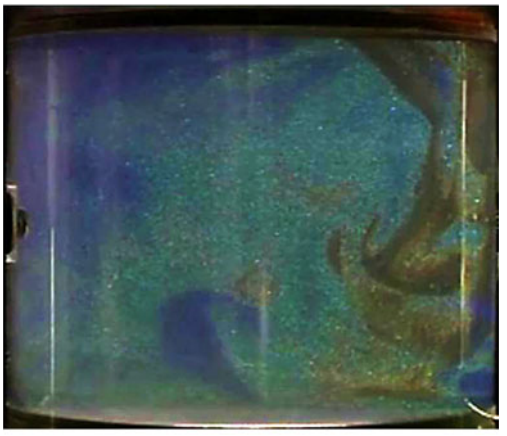

FIGURE 2. Flow visualization image of small TLC spheres taken in the $\Gamma = 1$ cell at $Ra = 3.7 \times 10^8$ and $Pr = 5.3$. Cold eruptions are brown; green and blue regions are warmer. The displayed region covers the entire convection cell and its physical dimension is approximately 10×10 cm^2.

through the middle section of the cylindrical cell. It is seen that falling cold plumes form bundle-like structures on the right and rising warm plumes bundle together on the left. The spatially separated warm and cold plumes exert buoyancy forces on the fluid and drive the vertical flow near the sidewall. The central core region is 'sheared' by the rising and falling plumes near the sidewall, resulting in a large-scale circulation across the cell height. This large-scale circulation provides a fast channel along the cell periphery for the transport of heat (Shang *et al.* 2004). The large-scale flow structure and plume distribution, as illustrated in figure 2, are generic features of turbulent RBC in the $\Gamma \simeq 1$ cylindrical cells, which have been studied extensively using different visualization techniques in various convecting fluids with the Rayleigh number in the range $10^8 \lesssim Ra \lesssim 10^{10}$ and the Prandtl number in the range of $4 \lesssim Pr \lesssim 1000$ (Shang *et al.* 2003; Sun *et al.* 2005; Xi & Xia 2008).

With this understanding of plume dynamics, we now discuss the scaling behaviour of the temperature–velocity CSFs and temperature SFs at two representative locations in the convection cell: at the cell centre and near the sidewall at the mid-height of the cell and 1 cm away from the cell wall. We find that the scaling properties of $S^n_{Tu}(\tau)$ and $S^n_T(r)$ remain unchanged in the Ra range studied. Hereafter, we focus on the results at fixed values of Ra. To determine whether temperature fluctuations at these two locations are a passive scalar, one needs to compare the Bolgiano scale L_B, above which buoyancy becomes significant, with the system size H. In fact, because both the viscous and thermal dissipation rates vary with the height z relative to the bottom surface of the cell, one needs to consider the local Bolgiano scale (Benzi, Toschi & Tripiccione 1998) $L_B(z) = (\alpha g)^{-3/2}[\epsilon_u(z)]^{5/4}[\epsilon_T(z)]^{-3/4}$, where $\epsilon_u(z)$ and $\epsilon_T(z)$ are, respectively, the energy and thermal dissipation rates averaged over the cross-section of the cell. In a numerical simulation at moderate Ra, Calzavarini *et al.* (2002) found that $L_B(z)$ is the smallest near the top and bottom plates and becomes the largest and comparable to H at the mid-height of the cell ($L_B(H/2)/H \simeq 0.88$). Thus, the temperature behaves like a passive scalar at these two locations. This conclusion was supported by early temperature and velocity measurements (Cioni *et al.* 1995;

Belmonte & Libchaber 1996; Chavanne *et al.* 2001; Sun *et al.* 2006) and also by recent measurements of the dissipation exponent (He *et al.* 2010*b*, 2011).

It should be noted that the scaling laws given in (1.1) and (1.2) (and their derivative given in (3.1) below) were made for isotropic turbulence, in which there is no preferred direction for the velocity vector $\boldsymbol{u}$ and displacement vector $\boldsymbol{r}$. This condition is satisfied approximately in the central region of the cell, in which the statistical properties of the convective flow are approximately isotropic (Zhou, Sun & Xia 2008) and the measured longitudinal velocity SF, where both $\boldsymbol{u}$ and $\boldsymbol{r}$ are along the same direction, and the traversal velocity SF, where $\boldsymbol{r}$ is perpendicular to $\boldsymbol{u}$, are found to be equal (Sun *et al.* 2006). The convective flow near the sidewall, however, is similar to a channel flow with a mean vertical velocity U_0 and a root-mean-square (r.m.s.) velocity $\sigma_u \simeq 0.6U_0$ (Qiu & Tong 2001). For those anisotropic flows such as turbulent channel flows and wakes and jets in wind tunnels, previous experimental and numerical studies (Saddoughi & Veeravalli 1994; Chen *et al.* 1997; Grossmann, Lohse & Reeh 1997) have shown that while the measured longitudinal and transversal velocity SFs are different, the obtained scaling exponent $\zeta_u^L(n)$ of the longitudinal SFs agree with the prediction given in (1.1). Therefore, in the present study we choose the axis of both r and u to be along the vertical direction, which is the longitudinal direction near the sidewall, and study the scaling properties of the longitudinal SFs and CSFs. Along the longitudinal direction, the effect of turbulent shear and sidewall is minimal.

3.1. *Scaling property of the temperature–velocity CSFs*

The temperature–velocity CSF, $S_{Tu}^n(\tau)$, is directly linked to the thermal dissipation rate $\epsilon_T(r)$. From (1.1) and (1.2), one can show that (Boratav & Pelz 1998)

$$S_{Tu}^n(r)r^{-n} \sim \langle[\epsilon_T(r)]^n\rangle. \tag{3.1}$$

In the above, we used the CSF $S_{Tu}^n(r)$ in the r-space. We now extend (3.1) from the r-space to the τ-domain with r being replaced by the delay time τ. Using (1.4), one can rewrite (3.1) in the exponent form

$$\zeta_{Tu}(n) - n = \mu(n), \tag{3.2}$$

where we have assumed $S_{Tu}^n(\tau) \sim \tau^{\zeta_{Tu}(n)}$. The validity of this assumption is checked below.

To link the τ-scaling with the r-scaling, a relationship between space and time is needed. Taylor's frozen flow hypothesis (Taylor 1938) provides such a relationship, but it requires that the mean flow velocity U_0 be much larger than velocity fluctuations. For turbulent RBC, however, the r.m.s. velocity σ_u is comparable with or even larger than U_0 (Qiu & Tong 2001), and thus this requirement is not met (Lohse & Xia 2010). Recently, He *et al.* (He & Zhang 2006; Zhao & He 2009) showed that for a spatially homogeneous and statistically stationary turbulent flow, the first-order terms in the Taylor series expansion of the velocity space–time correlation function $C_u(r, \tau)$ vanish and, therefore, $C_u(r, \tau)$ has a complete square form $C_u(r, \tau) = C_u(r_E, 0)$, where the combined space–time separation r_E between the two space–time points separated by a spatial distance r and time delay τ is given by

$$r_E^2 = (r - U_0\tau)^2 + V^2\tau^2, \tag{3.3}$$

where V is a random sweeping velocity proportional to σ_u. This elliptic relation between r and τ is exact up to the second order and may also hold for larger values of r and τ if the flow is scale-invariant. Equation (3.3) incorporates both the Taylor hypothesis when V is small and Kraichnan's random sweeping hypothesis (Kraichnan 1964) for an isotropic flow with $U_0 \simeq 0$.

This so-called elliptic model has been experimentally verified for $C_u(r, \tau)$ (Zhou *et al.* 2011) and for the temperature space–time correlation function $C_T(r, \tau)$ (He, He & Tong 2010*a*; He & Tong 2011; He *et al.* 2012) in turbulent RBC both at the cell centre and near the sidewall. Because the Taylor expansion and flow similarity assumption are quite general, the elliptic model is expected to be also valid for the temperature–velocity space–time cross-correlation function $C_{Tu}(r, \tau)$. There is an intrinsic correlation between $T(t)$ and $u_z(t)$ resulting from the local heat flux, which will make the function form of $C_{Tu}(r_E, 0)$ somewhat different from that of $C_T(r_E, 0)$ (and $C_u(r_E, 0)$). Because the heat flux is a local coincident event between $T(t)$ and $u_z(t)$ (for very small values of r and τ), the heat-flux-induced correlation should only affect the small-r_E behaviour of $C_{Tu}(r_E, 0)$. In this paper, we are interested in the scaling behaviour of the longitudinal SFs and CSFs in the inertial range, which takes place in the larger values of r_E (i.e. larger values of r and τ). Therefore, the heat-flux-induced correlation will most likely not affect the scaling exponent $\zeta_{Tu}(n)$ given in (3.2), which is verified experimentally as shown in figure 5 below.

Using (3.3) one can readily show that when $r = 0$ (single point measurement), one has $r_E = (U_0^2 + V^2)^{1/2}\tau = V_{eff}\tau$. This equation states that τ is statistically proportional to r near the sidewall and at the cell centre, even when the requirement of Taylor's frozen flow hypothesis is not met. This explains why the scaling exponent $\gamma_\tau(n)$ obtained from the extended self-similarity (ESS) scaling in τ has the same values as $\gamma_r(n)$ obtained from direct r-scaling, as shown in table 2 (see appendix A for more details).

To verify the scaling behaviour of $S^n_{Tu}(\tau)$, we use the ESS method (Benzi *et al.* 1993) to analyse the temperature–velocity CSFs. With ESS, one plots all of the moments $S^n_{Tu}(\tau)$ against the first moment $S^1_{Tu}(\tau)$ on log–log scales, which are shown in figure 3. From (3.1), one finds that $S^1_{Tu}(r) \sim r$ (or, equivalently, $S^1_{Tu}(\tau) \sim \tau$) (Yaglom 1949) and thus the plots shown in figure 3 are actually against τ (or r). Indeed, the scaling of $S^n_{Tu}(\tau)$ covers a wide range down to the dissipation time τ_η ($\simeq 6.4 \times 10^{-2}$ s) associated with the Komogorov length η, as indicated by the vertical dotted line in figure 3 (see appendix A for more details). A good power-law scaling is found for all $S^n_{Tu}(\tau)$ with n up to 4 (solid lines). For a common scaling region as marked by the two vertical dashed lines on the right, we use the least-squares method to fit all of the data and obtain the exponents $\zeta_{Tu}(n)$ from the equation,

$$S^n_{Tu}(\tau) \sim [S^1_{Tu}(\tau)]^{\zeta_{Tu}(n)} \sim \tau^{\zeta_{Tu}(n)}, \tag{3.4}$$

for all values of n up to 4. The measured values of $\zeta_{Tu}(n)$ are given in table 1. Owing to the wider scaling range in ESS, the uncertainties of the obtained $\zeta_{Tu}(n)$ are smaller than those obtained directly from the τ-scaling.

To check the accuracy of the obtained $\zeta_{Tu}(n)$, we examine the convergence level of the kernel function, $[\delta T^2_\tau \delta u_\tau/(\sigma^2_T \sigma_u)]^n P(\delta T^2_\tau \delta u_\tau)$, where σ_T and σ_u are the r.m.s. values of $\delta T(t)$ and $\delta u(t)$, and $P(\delta T^2_\tau \delta u_\tau)$ is the probability density function of $\delta T^2_\tau \delta u_\tau$. Figure 4 shows the obtained $[\delta T^2_\tau \delta u_\tau/(\sigma^2_T \sigma_u)]^n P(\delta T^2_\tau \delta u_\tau)$ at the lower end of the scaling range, $\tau = 1$ s for $n = 2$, 3, 3.5 and 4. It is seen that the kernel function converges well at large values of $\delta T^2_\tau \delta u_\tau$ for all values of n up to 3.5. For $n = 4$, the kernel function only converges partially because of its very slow converging rate.

	Sidewall				Centre		
n	$\zeta_T(n)$	$\gamma_r(n)$	$\gamma_\tau(n)$	$\gamma_\tau^u(n)$	$\zeta_T(n)$	$\gamma_r(n)$	$\gamma_\tau^u(n)$
0.5				0.27			0.31
1	0.30 ± 0.015	0.54 ± 0.01	0.59 ± 0.01	0.53	0.35 ± 0.01	0.60 ± 0.01	0.58
1.5				0.77			0.81
2	0.55 ± 0.025	1	1	1	0.60 ± 0.025	1	1
2.5				1.21			1.16
3	0.77 ± 0.03	1.39 ± 0.03	1.33 ± 0.03	1.41	0.73 ± 0.03	1.27 ± 0.02	
3.5				1.60			
4	0.95 ± 0.04	1.71 ± 0.04	1.61 ± 0.04	1.76	0.84 ± 0.04	1.47 ± 0.03	
5	1.10 ± 0.05	1.99 ± 0.05	1.87 ± 0.04		0.93 ± 0.05	1.63 ± 0.04	
6	1.22 ± 0.06	2.19 ± 0.06	2.09 ± 0.06		1.02 ± 0.06	1.77 ± 0.04	
7	1.32 ± 0.07	2.35 ± 0.07	2.29 ± 0.07		1.09 ± 0.07	1.91 ± 0.05	
8	1.42 ± 0.09	2.47 ± 0.08	2.47 ± 0.08		1.17 ± 0.09	2.06 ± 0.07	

TABLE 2. Summary of the obtained scaling exponents near the sidewall (first four columns) and at the cell centre (last three columns).

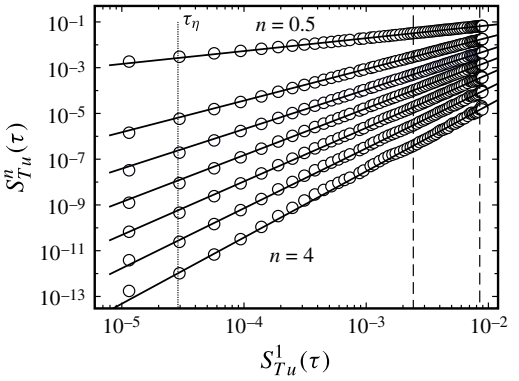

FIGURE 3. ESS plots of $S^n_{Tu}(\tau)$ as a function of $S^1_{Tu}(\tau)$ for 7 values of n from 0.5 to 4 with increments of 0.5 (top to bottom). All of the measurements were made near the sidewall at $Ra = 9.5 \times 10^9$. To display all of the curves in the same graph, the vertical scale of those curves with $n = 1.5$ to 3.5 has been multiplied by a factor of 10, 10, 9, 6, 3, respectively. The two vertical dashed lines on the right indicate the scaling range used to obtain $\mu(n)$ in He *et al.* (2011). The dotted line indicates the dissipation time $\tau_\eta \simeq 6.4 \times 10^{-2}$ s.

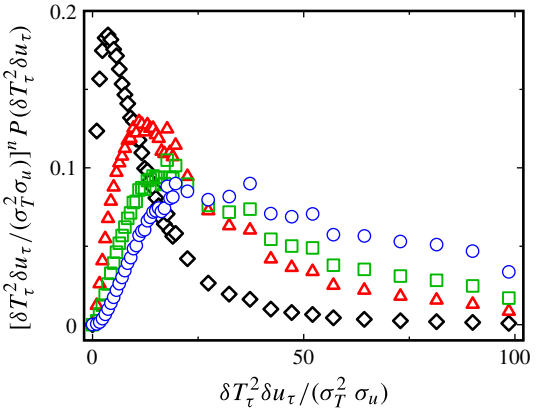

FIGURE 4. (Colour online) Obtained kernel function, $[\delta T_\tau^2 \delta u_\tau/(\sigma_T^2 \sigma_u)]^n P(\delta T_\tau^2 \delta u_\tau)$, for $n =$ 2 (black diamonds), 3 (triangles, red online) 3.5 (squares, green online) and 4 (circles, blue online) near the sidewall at $Ra = 9.5 \times 10^9$. The smallest value of τ (= 1 s) in the scaling range is used in the calculation. The vertical scale of the three curves with $n = 3$, 3.5 and 4 has been divided by a factor of 10, 50 and 250, respectively.

In figure 5, we make a direct comparison between the CSF exponent, $\zeta_{Tu}(n) - n$ (left-hand side of (3.2)), and the dissipation exponent $\mu(n)$ near the sidewall (figure 5*a*) and at the cell centre (figure 5*b*). The calculated values of $\zeta_{Tu}(n) - n$ from a direct numerical simulation (DNS) of isotropic passive-scalar turbulence with $Re_\lambda = 141$ and $Pr = 1$ (Boratav & Pelz 1998) are also included in figure 5(*b*). To expand the range of comparison, we calculate additional values of $\mu(n)$ for half-integers of n, which are also included in table 1. Because high-order temperature fluctuations are used in $\zeta_{Tu}(n)$ and $\mu(n)$, accurate determination of both $\zeta_{Tu}(n)$ and $\mu(n)$ is crucial for the comparison. While the kernel function with $n = 4$ only

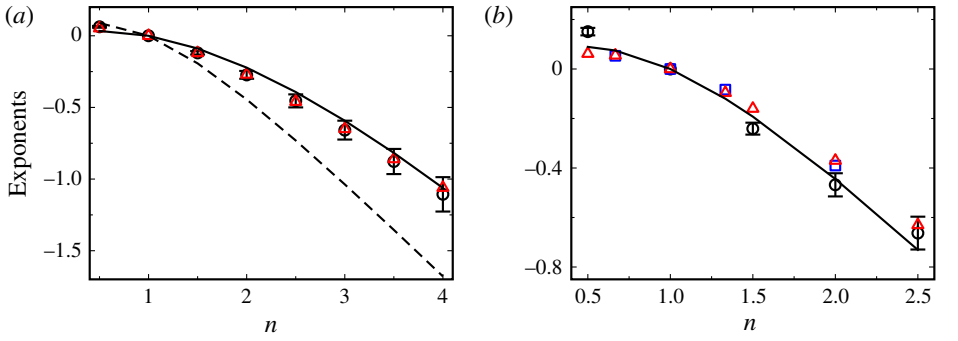

FIGURE 5. (Colour online) (*a*) Comparison between the exponents $\zeta_{Tu}(n) - n$ (black circles) and $\mu(n)$ (triangles, red online) as a function of n near the sidewall. Error bars are shown for black circles. The solid line is a plot of (3.5) with $c = 2$ and $\beta = 2/3$. The dashed line is a replot of the solid line in (*b*) for comparison. (*b*) Comparison between $\zeta_{Tu}(n) - n$ (black circles) and $\mu(n)$ (triangles, red online) at the cell centre. Error bars are shown for black circles. The squares (blue online) are the calculated $\zeta_{Tu}(n) - n$ from a DNS study (Boratav & Pelz 1998). The solid line is a plot of (3.5) with $c = 1$ and $\beta = 1/3$.

converges partially as shown in figure 4, we nonetheless include that data point in figure 5, which fits the curve smoothly but with a bigger error bar. Figure 5 reveals a good agreement between the exponents $\zeta_{Tu}(n) - n$ and $\mu(n)$ and thus demonstrates that the anomalous scaling in the temperature–velocity CSF is indeed caused by the spatial intermittency of the dissipation field.

Most phenomenological models on anomalous scaling were proposed for isotropic passive-scalar turbulence and thus they have no parameter to describe different local-flow properties of a spatially inhomogeneous flow (Lohse & Xia 2010). The model by She & Léveque (1994), however, has a unique feature that a geometric measure, namely the (fractal) dimension D_ϵ, is used to characterize the most dissipative structures in the flow. For a flow with spatial inhomogeneity, its most dissipative structures may have different values of D_ϵ at different locations. By assuming $\langle[\epsilon_T(\tau)]^n\rangle$ has a hierarchical structure of She–Léveque form (She & Léveque 1994), Ching *et al.* (Ching & Kwok 2000; He *et al.* 2010*b*, 2011) showed that the dissipation exponent $\mu(n)$ for passive scalars has the form

$$\mu(n) = c(1 - \beta^n) - \frac{2n}{3}, \tag{3.5}$$

where $0 < \beta < 1$ is a parameter to be determined by the condition $c(1 - \beta) - 2/3 = 0$, and $c = 3 - D_\epsilon$ is interpreted as the codimension of the most dissipative structures in the flow. The solid line in figure 5(*a*) is a plot of (3.5) with $c = 2$ and $\beta = 2/3$, suggesting the most dissipative structures near the sidewall are filament-like ($D_\epsilon = 1$). The solid line in figure 5(*b*) is a plot of (3.5) with $c = 1$ and $\beta = 1/3$, suggesting the most dissipative structures at the cell centre are sheetlike ($D_\epsilon = 2$). The data are described adequately by the two solid lines without any adjustable parameter. From the flow visualization, such as those shown in figure 2 and in Shang *et al.* (2003) and Xi & Xia (2008), one finds that the thermal plumes form bundle-like structures near the sidewall and they are fully mixed in the central region of the cell. Such a

characteristic change in the plume structures coincides with the geometry change of the most dissipative structures as discussed above. Figure 5 thus confirms that the geometry of the most dissipative structures at the cell centre differs from that near the sidewall, which explains the different functional form of the CSF exponents in the two regions.

3.2. *Scaling property of the temperature SFs*

Such a change in the geometry of the most dissipative structures may also be used to explain the two distinct behaviours of the reduced scaling exponent $\zeta_T(n)/\zeta_T(2)$, as shown in figure 1. To further verify the effect of spatial inhomogeneity on the temperature SFs, we conduct a systematic study of the scaling properties of $S_T^n(r)$ in turbulent RBC near the sidewall and at the cell centre. Details about this study are described in appendices A and B. Table 2 in appendix A summarizes the obtained values of the SF exponent $\zeta_T(n)$ near the sidewall and at the cell centre. From the obtained values of $\zeta_T(n)$, we calculate the reduced exponent $\zeta_T(n)/\zeta_T(2)$ and the final results are given in table 1. The solid squares (black) and solid circles (red online) in figure 1 show the values of the obtained $\zeta_T(n)/\zeta_T(2)$ near the sidewall and at the cell centre, respectively. The two new sets of data agree with those obtained previously (Sun *et al.* 2006) and the difference between them is clearly beyond the experimental uncertainties. The value of $\zeta_T(2)$ used in figure 1 varies from 0.55 near the sidewall to 0.6 at the cell centre. Previous experiments (Gylfason & Warhaft 2004) showed that $\zeta_T(2)$ varied in the range 0.45–0.68 for different turbulent flows. The use of the reduced exponent $\zeta_T(n)/\zeta_T(2)$ helps to reduce systematic errors in the experiment.

As shown in (3.1), the temperature–velocity CSF, $S_{Tu}^n(\tau)$, is uniquely determined by the scaling property of the thermal dissipation $\epsilon_T(r)$, which is well described by the hierarchical model as shown in (3.5). This equation is fully supported by the experimental data as shown in figure 5. Similarly, the velocity SF, $S_u^n(r)$, is uniquely determined by the scaling property of the viscous dissipation $\epsilon_u(r)$, as shown in (1.1). By assuming $\langle[\epsilon_u(r)]^n\rangle$ has a hierarchical structure, She & Léveque (1994) showed that the viscous dissipation exponent $\nu(n)$ in the equation,

$$\langle[\epsilon_u(r)]^n\rangle \sim r^{\nu(n)}, \tag{3.6}$$

has the same form as shown in (3.5). By further assuming that the most dissipative structures in the velocity field are filament-like ($c = 2$), She & Léveque (1994) predicted

$$\nu(n) = 2\left[1 - \left(\tfrac{2}{3}\right)^n\right] - \tfrac{2}{3}n, \tag{3.7}$$

for positive values of n. From (1.1) and (3.7), one finds

$$\zeta_u(n) = \nu(n/3) + \frac{n}{3} = 2\left[1 - \left(\frac{2}{3}\right)^{n/3}\right] + \frac{n}{9}. \tag{3.8}$$

Equation (3.8) was verified with the measured velocity SF exponent in a turbulent grid flow and a turbulent jet in a wind tunnel (Benzi *et al.* 1993). For turbulent RBC, both our single-point time series data and previous space-resolved particle-image-velocimetry (PIV) data obtained by Sun *et al.* (2006) reveal that the reduced exponent $\zeta_u(n)/\zeta_u(2)$ at the cell centre remains the same as that near the sidewall and both sets of data can be well described by (3.8) (see figure 12 in appendix C for more details). These results thus suggest that the most dissipative structures of the

velocity field in turbulent RBC are filament-like ($c_u = 2$) and they remain the same across the convection cell.

Unlike the velocity SF and temperature–velocity CSF, the temperature SF is determined by the scaling properties of both the viscous dissipation $\epsilon_u(r)$ and thermal dissipation $\epsilon_T(r)$, as shown in (1.2). Owing to the correlation between the two dissipation fields, those proposals that assume the temperature SF, $S_T^n(r)$, has a unform hierarchical structure (Ruiz-Chavarria *et al.* 1996) need a further physical justification, in order to address the coupling effect between the two dissipation fields. Up to now, we do not have an analytical theory or direct experimental evidence to estimate how important the higher-order dissipation correlations are. Nevertheless, attempts were made to develop approximate models for $S_T^n(r)$ (Lohse & Xia 2010). While various functional forms have been used to fit the reduced exponent $\zeta_T(n)/\zeta_T(2)$ (Ruiz-Chavarria *et al.* 1996; Gylfason & Warhaft 2004), herein we focus our discussion on those phenomenological models, which directly involved with the scaling properties of both $\epsilon_u(r)$ and $\epsilon_T(r)$. In the above, we have thoroughly tested the scaling properties of $\epsilon_u(r)$ and $\epsilon_T(r)$, and now we compare the model predictions made under different approximations with the experiment.

(*a*) When the correlation between the two dissipation fields is weak, one may assume $\langle \epsilon_u(r)^{-n/6} \epsilon_T(r)^{n/2} \rangle \sim \langle \epsilon_u(r)^{-n/6} \rangle \langle \epsilon_T(r)^{n/2} \rangle$. Attempt has been made to test this weak correlation assumption (Ruiz-Chavarria *et al.* 1996). To calculate the scaling property of $\langle \epsilon_u(r)^{-n/6} \rangle$, Cao & Chen (1997) extended the calculation of $\nu(+n)$ in (3.7) and obtained an expression for $\nu(-n)$ with $n > 0$:

$$\nu(-n) = 2\left[1 - \left(\tfrac{4}{3}\right)^{-n}\right] + \tfrac{2}{3}(-n). \tag{3.9}$$

Putting (1.2), (3.5) and (3.9) together, we find

$$\begin{aligned} \zeta_T^A(n) &= \nu(-n/6) + \mu(n/2) + \frac{n}{3} \\ &= 2\left[1 - \left(\frac{4}{3}\right)^{-n/6}\right] + c\left[1 - \left(1 - \frac{2}{3c}\right)^{n/2}\right] - \frac{n}{9}. \end{aligned} \tag{3.10}$$

(*b*) Similarly, if the correlation between the velocity and temperature fields is weak, one may assume $S_{Tu}^n(r) \sim S_T^{2n}(r) S_u^n(r)$. Using the simultaneously taken data of the vertical velocity $u_z(t)$ and local temperature $T(t)$, we examine the correlation between $u_z(t)$ and $T(t)$ in the time domain. The final results are presented in appendix C. Putting (1.1), (1.2), (3.5) and (3.9) together, we find

$$\begin{aligned} \zeta_T^B(n) &= -\nu(n/6) + \mu(n/2) + \frac{n}{3} \\ &= -2\left[1 - \left(\frac{2}{3}\right)^{n/6}\right] + c\left[1 - \left(1 - \frac{2}{3c}\right)^{n/2}\right] + \frac{n}{9}. \end{aligned} \tag{3.11}$$

Equations (3.10) and (3.11) reveal the effect of the double intermittency corrections on the SF exponent $\zeta_T(n)$.

Figure 6 shows a comparison between the experimental data and various model predictions. For clarity, we plot only two sets of the measured scaling exponents $\zeta_T(n)/\zeta_T(2)$, which are obtained in the present experiment on turbulent RBC near the sidewall (open squares, black) and at the cell centre (open circles, red online). They

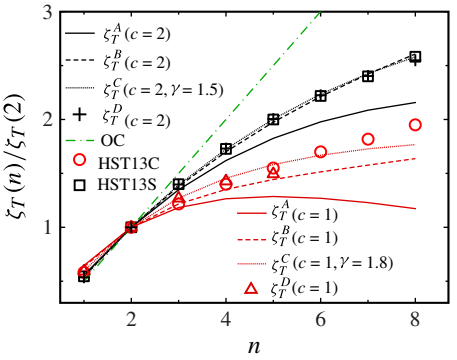

FIGURE 6. (Colour online) Reduced scaling exponent $\zeta_T(n)/\zeta_T(2)$ as a function of n obtained in turbulent RBC near the sidewall (HST13S, open squares, black) and at the cell centre (HST13C, open circles, red online). The dot–dashed (green online) line is the classical Obukhov–Corrsin scaling, $\zeta_T(n) = n/3$, without any intermittency correction. The lower solid and dashed (red online) lines are, respectively, the plots of (3.10) $[\zeta_T^A(n)]$ and (3.11) $[\zeta_T^B(n)]$ with $c = 1$. The upper solid and dashed lines (black) are, respectively, the plots of (3.10) $[\zeta_T^A(n)]$ and (3.11) $[\zeta_T^B(n)]$ with $c = 2$. The upper dotted (black) line and lower dotted (red online) line are the plots of (3.13) $[\zeta_T^C(n)]$ with $c = 2$, $\gamma = 1.5$ and $c = 1$, $\gamma = 1.8$, respectively. The black crosses and red triangles are the plots of (3.16) $[\zeta_T^D(n)]$ near the sidewall and at the cell centre, respectively.

are chosen to represent the two distinct behaviours of the measured $\zeta_T(n)/\zeta_T(2)$, as shown in figure 1. The (green online) dot–dashed line shows the classical Obukhov–Corrsin scaling, $\zeta_T(n) = n/3$, without any intermittency correction (Obukhov 1949; Corrsin 1951). It is seen that the measured $\zeta_T(n)$ is not a linear function of n, as predicted by the Obukhov–Corrsin scaling. Instead, it curves down at large values of n, which was attributed to the spatial intermittency of the dissipation fields (Lohse & Xia 2010). The solid and dashed lines are, respectively, the plots of (3.10) $[\zeta_T^A(n)]$ and (3.11) $[\zeta_T^B(n)]$ with $c = 1$ (lower curves, red online) and $c = 2$ (upper curves, black). It is seen that while both (3.10) and (3.11) can fit the data at small values of n ($\lesssim 3$), deviations between the model predictions and experimental data become larger with increasing values of n. In particular, the solution $\zeta_T^A(n)$ of (3.10) with $c = 1$ (lower solid line, red online) shows the largest deviation when compared with the data at the cell centre. On the other hand, the solution $\zeta_T^B(n)$ of (3.11) with $c = 2$ (upper dashed line, black) fits the sidewall data well. A main difference between $\zeta_T^A(n)$ and $\zeta_T^B(n)$ is that for large values of n, $\zeta_T^A(n) \to -n/9$ whereas $\zeta_T^B(n) \to +n/9$. As shown in figure 6, the measured $\zeta_T(n)/\zeta_T(2)$ keeps increasing with n even at large values of n, which explains why (3.11) fits the data better than (3.10) in general.

(*c*) We now consider the correlation effect between the viscous dissipation $\epsilon_u(r)$ and thermal dissipation $\epsilon_T(r)$. This issue has been considered previously by Cao & Chen (1997) and He, Chen & Doolen (1998). Assuming that

$$\langle \epsilon_u(r)^{-n/6} \epsilon_T(r)^{n/2} \rangle = \langle \epsilon_u(r)^{-n/6} \rangle \langle \epsilon_T(r)^{n/2} \rangle r^{\theta(-n/6,n/2)}, \tag{3.12}$$

and using (3.10), we find a new solution for the temperature SF exponent $\zeta_T^C(n)$ with a correlation correction,

$$\zeta_T^C(n) = \zeta_T^A(n) + \theta(-n/6, n/2), \tag{3.13}$$

where

$$\theta(-n/6, n/2) = \gamma \left[1 - \left(\frac{4}{3}\right)^{-n/6} - \left(\frac{2}{3c}\right)^{n/2} + \left(\frac{4}{3}\right)^{-n/6}\left(\frac{2}{3c}\right)^{n/2}\right]. \tag{3.14}$$

Equation (3.14) was derived by assuming the correlation between $\epsilon_u(r)$ and $\epsilon_T(r)$ obeys a joint Poisson distribution (Cao & Chen 1997; He *et al.* 1998). In (3.14), γ is a free parameter and is chosen to best fit the data. The upper dotted (black online) line and lower dotted (red online) line shown in figure 6 are the plots of (3.13) with $c = 2$, $\gamma = 1.5$ and $c = 1$, $\gamma = 1.8$, respectively. The corresponding values of $\theta(-n/6, n/2)$ are listed in table 1. With a free fitting parameter, the correlation-corrected solution $\zeta_T^C(n)$ can give a better fit than $\zeta_T^A(n)$. In fact, the obtained $\zeta_T^C(n)$ curve with $c = 2$ is very close to $\zeta_T^B(n)$; both can fit the data well. For $c = 1$, however, small deviations between the calculated $\zeta_T^C(n)$ and the experimental data are observed for large values of n ($\gtrsim 6$). This is partially caused by the fact that at the large n limit, $\zeta_T^C(n) \to -n/9$, a trend which is inconsistent with the data shown in figure 6.

(*d*) Similarly, we consider the correction to $\zeta_T^B(n)$ due to the correlation between δu_r^n and δT_r^{2n}. Assuming that

$$\langle \delta u_r^n \delta T_r^{2n} \rangle = \langle \delta u_r^n \rangle \langle \delta T_r^{2n} \rangle r^{\phi(n,2n)}, \tag{3.15}$$

and using (3.1) and (3.11), we find a new solution for the SF exponent $\zeta_T^D(n)$ with a correlation correction,

$$\zeta_T^D(n) = \zeta_T^B(n) - \phi(n/2, n). \tag{3.16}$$

In appendix C, we calculate the numerical values of $\phi(n, 2n)$ using the simultaneously taken time series data of the vertical velocity $u_z(t)$ and local temperature $T(t)$. The final results are given in table 1. It is found that the correlation between the velocity moments δu_τ^n and temperature moments δT_τ^{2n} is weak near the sidewall, and the obtained values of $\phi(n, 2n)$ are very small (close to zero) for all values of n up to 4. The correlation becomes stronger at the cell centre and the obtained value of $\phi(n, 2n)$ increases with n. The black crosses in figure 6 show the values of $\zeta_T^D(n)$ obtained using (3.16) with the values of $\phi(n, 2n)$ near the sidewall given in table 1. It is seen that the solution $\zeta_T^D(n)$ is in excellent agreement with the sidewall data. Because the values of $\phi(n, 2n)$ are very small, the correlation correction to $\zeta_T^B(n)$ is also small. This explains why the solution $\zeta_T^B(n)$ in (3.11) with $c = 2$ (upper dashed line, black) also fits the sidewall data well. The triangles (red online) in figure 6 show the values of $\zeta_T^D(n)$ obtained using (3.16) with the values of $\phi(n, 2n)$ at the cell centre given in table 1. It is seen that the obtained values of $\zeta_T^D(n)$ also agree well with the experimental data at the cell centre. Because the values of $\phi(n, 2n)$ are all negative, the final correlation correction to $\zeta_T^B(n)$ is positive. Figure 6 thus suggests that among the solutions (*a*)–(*d*) predicted by different phenomenological models, the solution $\zeta_T^D(n)$ in (3.16) gives a more accurate description of the measured temperature SF exponent with a minimum number of input parameters or presumptions.

4. Summary

Over the past decades, continuing efforts have been made to understand the scaling properties of temperature and velocity fluctuations in turbulent RBC. Many experiments focused on the power spectra and SFs of local temperature and velocity fluctuations. The interpretation of the experimental results, however, are often

complicated by other effects in the convective flow, such as flow anisotropy and inhomogeneity, determination of the Bolgiano scale, the validity of using Taylor's frozen flow hypothesis to analyse the single-point measurements, and lack of spatial separation of the relevant length scales for the flow in a closed convection cell (Lohse & Xia 2010). More recently, with a concerted effort of DNS (Calzavarini *et al.* 2002; Kunnen *et al.* 2008) and space-resolved measurements of temperature and velocity SFs (Sun *et al.* 2006), space–time cross-correlation functions (He *et al.* 2010*a*; He & Tong 2011), and local thermal dissipation rate (He *et al.* 2010*b*, 2011), many of the experimental complications have been resolved.

Based on this collective understanding, we have carried out a careful analysis on the scaling properties of the temperature SF $S_T^n(r)$ and temperature–velocity CSF $S_{Tu}^n(\tau)$. The measured $S_T^n(r)$ and $S_{Tu}^n(\tau)$ are found to exhibit good scaling in space r and time τ and the resulting exponents $\zeta_T(n)$ and $\zeta_{Tu}(n)$ are obtained at the cell centre and near the sidewall; at both locations the temperature behaves like a passive scalar. With the aid of the previously measured scaling exponent $\mu(n)$ of the local thermal dissipation rate (He *et al.* 2010*b*, 2011), we make a direct comparison between the CSF exponent $\zeta_{Tu}(n) - n$ and the dissipation exponent $\mu(n)$ via (3.2). An excellent agreement between the measured $\zeta_{Tu}(n) - n$ and $\mu(n)$ is observed both at the cell centre and near the sidewall, as shown in figure 5. The experiment thus demonstrates for the first time that the anomalous scaling of passive temperature fluctuations is indeed caused by the scale-dependent statistics of the dissipation field. It is also found that the difference in the functional form of the measured $\zeta_{Tu}(n)$ at the two different locations in the convection cell is caused by the change of the geometry of the most dissipative structures in the (inhomogeneous) temperature field from being sheetlike ($c_T = 1$) at the cell centre to filament-like ($c_T = 2$) near the sidewall.

With these new findings, we conduct a detailed comparison between the measured $\zeta_T(n)$ in turbulent RBC and those obtained in other locally homogeneous turbulent flows, such as grid turbulence (Gylfason & Warhaft 2004; Lepore & Mydlarski 2009) and heated jet (Antonia *et al.* 1984) and wake (Meneveau *et al.* 1990; Ruiz-Chavarria *et al.* 1996). The whole body of data as shown in figure 1 clearly reveal two distinct behaviours of $\zeta_T(n)$, with turbulent RBC near the sidewall belonging to one group and the rest of the data sets being the other group. These two different behaviours, which clearly demonstrate the effect of spatial inhomogeneity of turbulence on the temperature SFs, are explained by a phenomenological model given in (3.16). A good agreement between the model prediction and the measured $\zeta_T(n)$ is observed, when the codimension c_T of the most dissipative structures in the temperature field is assumed to be changed from sheetlike ($c_T = 1$) at the cell centre to filament-like ($c_T = 2$) near the sidewall. The experiment thus provides direct evidence showing that the universality features of turbulent cascade are linked to the degree of anisotropy and inhomogeneity of turbulent statistics (Biferale & Procaccia 2005; Arnèodo *et al.* 2008).

By comparing different phenomenological models on the anomalous scaling of passive scalars, we find that (3.16) gives a more accurate description of the measured $\zeta_T(n)$ with a minimum number of input parameters or presumptions. It is interesting to note that at the cell centre, the codimension c_u of the most dissipative structures in the velocity field is the same as that of the temperature field c_T, both of them being sheetlike-like ($c_u = c_T = 1$), and a strong correlation between the velocity moments δu_τ^n and temperature moments δT_τ^{2n} is observed. This correlation is found to increase with the order n of the moments. Near the sidewall, however, the most dissipative structures in the velocity field remain to be sheetlike ($c_u = 2$) but the most dissipative structures in the temperature field becomes filament-like ($c_T = 1$). In this case, the correlation between δu_τ^n and δT_τ^{2n} is found to be very weak.

Acknowledgements

We have benefitted from illuminating discussions with E. Ching, K. Xia and Z. She. We thank H. Song for his work in producing the flow visualization images. This work was supported by RGC of Hong Kong SAR under grant number HKUST-605013 (PT) and in part by NSFC under grant numbers XDA11010202 and U1033002 (XDS).

Appendix A. Temperature SFs near the sidewall

Figure 7(*a*) shows the compensated plot of the temperature SFs, $S_T^n(r)/r^{\zeta_T(n)}$, as a function of r/η for $n = 3$, 5 and 8 (bottom to top). In the plot, r is scaled by the Kolmogorov dissipation length, $\eta = HPr^{1/2}/[NuRa]^{1/4}$ (Cioni *et al.* 1995), where Nu is the Nusselt number (normalized heat flux). Using the measured $Nu = 0.17Ra^{0.29}$ in a similar convection system (Du & Tong 2000), we find $\eta \simeq 0.35$ mm at $Ra = 1.4 \times 10^{10}$ (He *et al.* 2011). The flat region of $S_T^n(r)/r^{\zeta_T(n)}$ reveals the good power-law scaling for all $S_T^n(r)/r^{\zeta_T(n)}$ with n up to 8 (solid lines). The scaling range in r is slightly over a decade long between 4η and 50η. For a common scaling region in r, we use the least-squares method to fit all of the data and obtain $\zeta_T(n)$ for different values of n up to 8. The measured values of $\zeta_T(n)$ are given in table 2.

Because the scaling range in r is short, the obtained $\zeta_T(n)$ is known to have relatively large uncertainties. In the present experiment, great care was taken to properly align the two thermistors and to vary r with a high spatial resolution. To check the accuracy of the obtained $\zeta_T(n)$, we examine the convergence level of the kernel function, $(\delta T_r/\sigma_T)^n P(\delta T_r)$, where the temperature increment δT_r is normalized by its r.m.s. value σ_T and $P(\delta T_r)$ is the probability density function of δT_r. Figure 7(*b*) shows the obtained $(\delta T_r/\sigma_T)^n P(\delta T_r)$ at the lower end of the scaling range, $r = 1.1$ mm, for $n = 4$, 6 and 8. It is seen that the kernel function converges well at large absolute values of $\delta T_r/\sigma_T$ for all values of n up to 8. Because the measured $P(\delta T_r)$ near the sidewall is asymmetric with a long tail in the $\delta T_r < 0$ region, the convergence of $(\delta T_r/\sigma_T)^n P(\delta T_r)$ in the $\delta T_r < 0$ region is slower than that in the $\delta T_r > 0$ region.

To further verify the scaling behaviour of $S_T^n(r)$, we use the ESS method (Benzi *et al.* 1993) to analyse the temperature SFs. With ESS, one plots all of the moments $S_T^n(r)$ against the second moment $S_T^2(r)$ on log–log scales, which are shown in figure 8(*a*). Indeed, the scaling of $S_T^n(r)$ covers a wider range down to the Komogorov length η (vertical dashed line). From the slope of the ESS plots, we obtain the exponent $\gamma_r(n)$ from the equation,

$$S_T^n(r) = [S_T^2(r)]^{\gamma_r(n)} \sim r^{\zeta_T(2)\gamma_r(n)}. \tag{A 1}$$

The measured values of $\gamma_r(n)$ are given in table 2. By comparing (A 1) with (1.2), one immediately finds $\zeta_T(n) = \zeta_T(2)\gamma_r(n)$. Owing to the wider scaling range in ESS, the uncertainties of the obtained $\gamma_r(n)$ are smaller than those for $\zeta_T(n)$.

Similar to the SF in space, one can also defined a temperature SF in the time domain (Ching & Kwok 2000), $S_T^n(\tau) = \langle [T(t+\tau) - T(t)]^n \rangle_t = \langle \delta T_\tau^n \rangle$, where δT_τ is obtained from the single-point time series measurement. Figure 8(*b*) shows the compensated ESS plots of the measured $S_T^n(\tau)/[S_T^2(\tau)]^{\gamma_\tau(n)}$ as a function of $S_T^2(\tau)$ for $n = 3$, 4, 6 and 8 (bottom to top). The flat region of $S_T^n(\tau)/[S_T^2(\tau)]^{\gamma_\tau(n)}$ reveals the good power-law scaling against $S_T^2(\tau)$ for all values of n up to 8. It is found that the scaling range of $S_T^n(\tau)/[S_T^2(\tau)]^{\gamma_\tau(n)}$ in the ESS plots starts at $\tau \simeq 6.4\tau_\eta$ (left) and ends at $\tau \simeq 19.1\tau_\eta$ (right), which are marked by the two vertical dashed (blue online) lines in figure 8(*b*). Here τ_η is the dissipation time associated with the Kolmogorov

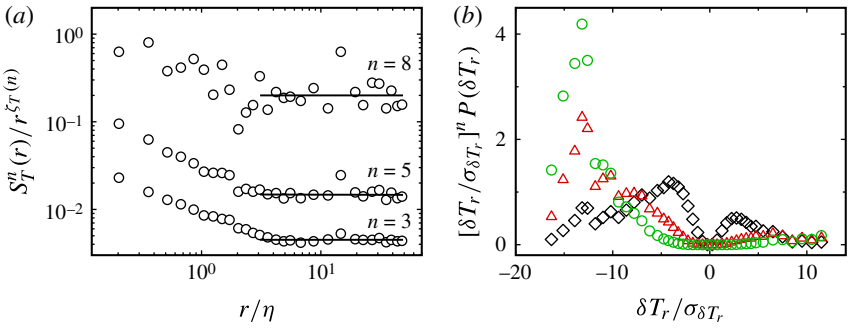

FIGURE 7. (Colour online) (*a*) Compensated plots, $S_T^n(r)/r^{\zeta_T(n)}$, as a function of r/η for $n=3$, 5 and 8 (bottom to top). To display all of the curves in the same graph, the vertical scales for $n=5$ and $n=8$ have been reduced by a factor of 10 and 10^2, respectively. (*b*) Obtained kernel function, $(\delta T_r/\sigma_T)^n P(\delta T_r)$, for $n=4$ (diamonds, black), 6 (triangles, red online) and 8 (circles, green online). The smallest value of r ($=1.1$ mm) in the scaling range is used in the calculation. The vertical scales for $n=4$ and $n=6$ have been reduced by a factor of 50 and 5000, respectively. Both of the data in (*a*) and (*b*) were obtained near the sidewall at $Ra=1.4\times10^{10}$.

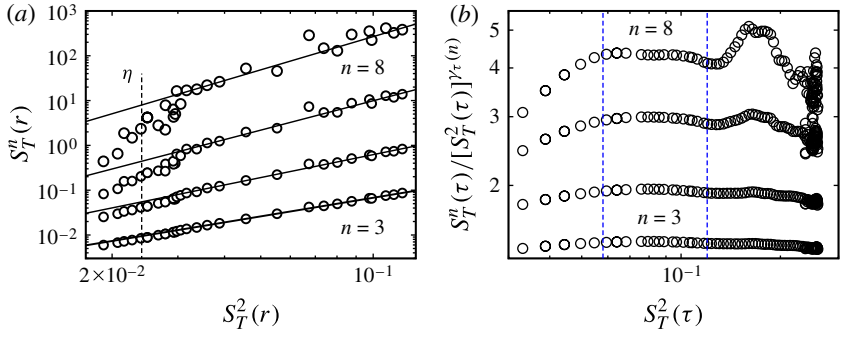

FIGURE 8. (Colour online) (*a*) ESS plots of $S_T^n(r)$ as a function of $S_T^2(r)$ for $n=3$, 4, 6 and 8 (bottom to top). The vertical scales for $n=4$, 6 and 8 have been multiplied by a factor of 10, 10^2 and 10^3, respectively. The vertical dashed line indicates the estimated Kolmogorov length $\eta\simeq0.35$ mm. (*b*) Compensated ESS plots of $S_T^n(\tau)/\left[S_T^2(\tau)\right]^{\gamma_\tau(n)}$ as a function of $S_T^2(\tau)$ for $n=3$, 4, 6 and 8 (bottom to top). The vertical scales for $n=4$, 6 and 8 have been reduced by a factor of 1.2, 3 and 12, respectively. The vertical dashed (blue online) lines indicate the scaling range from $\tau=6.4\tau_\eta$ (left) to $\tau=19.1\tau_\eta$ (right) with the estimated Kolmogorov time $\tau_\eta\simeq4.7\times10^{-2}$ s. All of the measurements were conducted near the sidewall with $Ra=1.4\times10^{10}$.

length η, which can be estimated as $\tau_\eta\simeq\tau_0\eta/H$ (Ching *et al.* 2003), where $\tau_0=4H^2/(1.1Ra^{0.45}\kappa)$ is the turnover time of the large-scale circulation observed in a similar system (Qiu & Tong 2001). For $Ra=1.4\times10^{10}$, we find $\tau_0=27.3$ s and $\tau_\eta=4.7\times10^{-2}$ s. From the slope of the ESS plots, we obtain the power-law exponent $\gamma_\tau(n)$ from the equation,

$$S_T^n(\tau)=[S_T^2(\tau)]^{\gamma_\tau(n)}\sim\tau^{\zeta_T(2)\gamma_\tau(n)}. \tag{A 2}$$

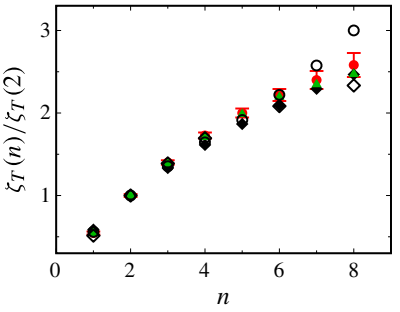

FIGURE 9. (Colour online) Reduced scaling exponent $\zeta_T(n)/\zeta_T(2)$ as a function of n near the sidewall at $Ra \simeq 1.4 \times 10^{10}$. The values of $\zeta_T(n)/\zeta_T(2)$ are obtained by direct r-scaling (solid circles, red online), ESS scaling in r (solid triangles, green online) and ESS scaling in τ (solid diamonds, black). Error bars are shown for (red online) solid circles. For comparison, the results by Sun *et al.* (2006) (black open circles) and by Skrbek *et al.* (2002) (black open diamonds) are also included.

The measured values of $\gamma_\tau(n)$ are given in table 2. From table 2 we find that within the experimental uncertainties $\gamma_\tau(n) \simeq \gamma_r(n)$ for all values of n up to 8.

Figure 9 shows the reduced scaling exponent $\zeta_T(n)/\zeta_T(2)$ obtained in three different ways: direct r-scaling (solid circles, red online), ESS scaling in r (solid triangles, green online) and ESS scaling in τ (solid diamonds, black). In the latter two cases, we used $\gamma_r(n)$ and $\gamma_\tau(n)$ as the reduced scaling exponent. It is seen that the three sets of data superimpose very well. For comparison, we also include, in figure 9, the measured $\zeta_T(n)/\zeta_T(2)$ near the sidewall from two previous experiments. One was carried out in low-temperature helium gas and $\gamma_\tau(n)$ was obtained by Skrbek *et al.* (2002). The other experiment was conducted in water and the values of $\zeta_T(n)$ were obtained from direct r-scaling (Sun *et al.* 2006). The five sets of data agree with each other very well for $n \leqslant 5$. For $n \geqslant 6$, the measured $\zeta_T(n)/\zeta_T(2)$ by Sun *et al.* (2006) become increasingly larger than the other measurements. Such a deviation may result from the experimental uncertainties in the direct r-scaling, which are magnified at large values of n. Other systematic errors were also found for the scaling exponents in several known multiplicative cascade processes (Lashermes, Abry & Chainais 2004), which indicates that the asymptotic behaviour of $\zeta_T(n)$ at very large values of n needs to be dealt with care. Figure 9 clearly reveals that the measured $\zeta_T(n)$ is not a linear function of n, which was attributed to the spatial intermittency of the dissipation field (Lohse & Xia 2010).

Appendix B. Temperature SFs at the cell centre

Similarly, we apply the same procedures and rigor to analyse the temperature SFs at the cell centre. Figure 10(*a*) shows the compensated plots, $S_T^n(r)/r^{\zeta_T(n)}$, as a function of r/η for $n = 3$, 5 and 8 (bottom to top). The obtained $S_T^n(r)/r^{\zeta_T(n)}$ reveals a good power-law scaling in r, as indicated by the plateau region in the plot (solid lines). The scaling range is slightly over a decade long ranging from $\sim 4\eta$ to 60η. Using the least-squares fitting method, we obtain the scaling exponent $\zeta_T(n)$ for different n. The measured values of $\zeta_T(n)$ are given in table 2. Figure 10(*b*) shows the ESS plots of $S_T^n(r)$ as a function of $S_T^2(r)$ for $n = 3$, 4, 6 and 8 (bottom to top). Similar to the situation near the sidewall, the measured $S_T^n(r)$ at the cell centre also reveals good ESS

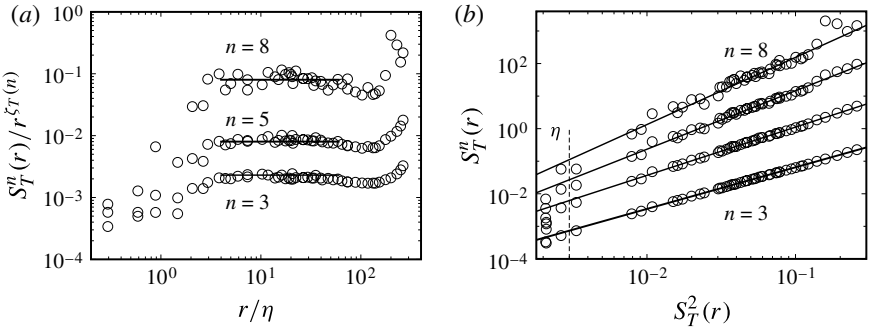

FIGURE 10. (*a*) Compensated plots, $S_T^n(r)/r^{\zeta_T(n)}$ versus r/η for $n = 3$, 5 and 8 (bottom to top). The vertical scales for $n = 5$ and $n = 8$ have been reduced by a factor of 10 and 10^2, respectively. (*b*) ESS plots of $S_T^n(r)$ as a function of $S_T^2(r)$ for $n = 3$, 4, 6 and 8 (bottom to top). The vertical scales for $n = 4$, 6 and 8 have been multiplied by a factor of 20, 200 and 2000, respectively. The vertical dashed line indicates the Kolmogorov length $\eta \simeq 0.33$ mm. All the measurements were made at the cell centre with $Ra \simeq 1.7 \times 10^{10}$. The solid lines indicate the power-law region.

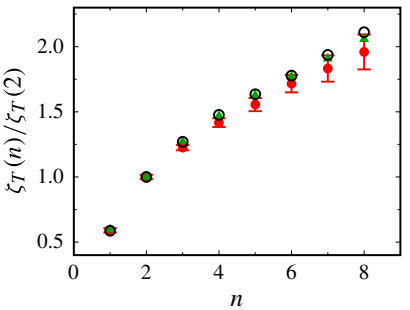

FIGURE 11. (Colour online) Reduced scaling exponent $\zeta_T(n)/\zeta_T(2)$ as a function of n at the cell centre with $Ra = 1.7 \times 10^{10}$. The values of $\zeta_T(n)$ are obtained by direct r-scaling (solid circles, red online) and ESS scaling in r (solid triangles, green online). Error bars are shown for (red online) solid circles. For comparison, the results by Sun *et al.* (2006) (open circles, black) are also included.

scaling, which covers a wider range down to the dissipation length η (vertical dashed line). The increase in the scaling range reduces the uncertainties of the measured $\gamma_r(n)$. The values of $\gamma_r(n)$ are given in table 2.

Figure 11 shows the reduced scaling exponent $\zeta_T(n)/\zeta_T(2)$ at the cell centre obtained in two different ways: direct r-scaling (solid circles, red online) and ESS scaling in r (solid triangles, green online). In the latter case, we used $\gamma_r(n)$ as the reduced scaling exponent. It is seen that the two sets of data superimpose very well. For comparison, we also include the measured $\zeta_T(n)/\zeta_T(2)$ at the cell centre from a previous convection experiment (Sun *et al.* 2006). The three sets of data agree well with each other within the experimental uncertainties. Note that there is a small but systematic deviation between the measured $\zeta_T(n)$ in the present experiment and that by Sun *et al.* (2006) (see table 2). The use of the reduced exponent $\zeta_T(n)/\zeta_T(2)$ helps to reduce the systematic errors in the experiments.

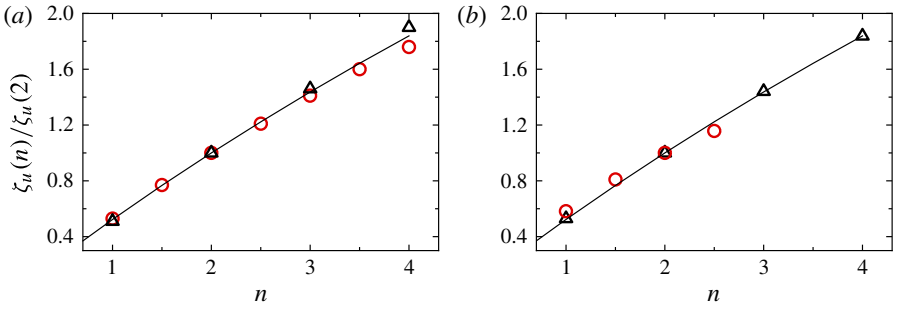

FIGURE 12. (Colour online) (*a*) Reduced scaling exponent $\zeta_u(n)/\zeta_u(2)$ as a function of n near the sidewall at $Ra = 9.5 \times 10^9$. (*b*) Measured $\zeta_u(n)/\zeta_u(2)$ as a function of n at the cell centre with $Ra = 1.4 \times 10^{10}$. The values of $\zeta_u(n)$ used in (*a*) and (*b*) are obtained by ESS scaling in τ (circles, red online). For comparison, the space-resolved PIV data by Sun *et al.* (2006) are also included (triangles, black). The solid lines are the plot of (3.8).

Appendix C. Correlations between the temperature and velocity SFs

Using the simultaneously taken time series data of the vertical velocity $u_z(t)$ and local temperature $T(t)$ at the cell centre and near the sidewall, one can study the scaling properties of the temperature SF $\langle \delta T_\tau^n \rangle$, velocity SF $\langle \delta u_\tau^n \rangle$ and their CSF $\langle \delta u_\tau^n \delta T_\tau^{2n} \rangle$ individually. We first study the τ-scaling of $\langle \delta T_\tau^n \rangle$ and $\langle \delta u_\tau^n \rangle$. Following the same procedure as discussed in appendix A, we use the ESS method (Benzi *et al.* 1993) to analyse the temperature and velocity SFs. With ESS, we plot all of the moments $S_T^n(\tau)$ (and $S_u^n(\tau)$) against the second moment $S_T^2(\tau)$ (or $S_u^2(\tau)$) on log–log scales, and find a good scaling range of $S_T^n(\tau)$ (and $S_u^n(\tau)$) for all cases. From the slope of the ESS plots, we obtain the exponent $\gamma_\tau(n) = \zeta_T(n)/\zeta_T(2)$ from (A 2). The obtained values of $\gamma_\tau(n)$ are found to be the same as those discussed in appendices A and B, indicating that the temperature statistics of this set of data remain the same as those discussed in appendices A and B.

Similarly, we obtain the velocity SF exponent $\gamma_\tau^u(n) = \zeta_u(n)/\zeta_u(2)$ and its numerical values are given in table 2. Figure 12(*a*) shows the reduced exponent $\zeta_u(n)/\zeta_u(2)$ near the sidewall (circles, red online). For comparison, we also include the obtained $\zeta_T(n)/\zeta_T(2)$ near the sidewall from a previous experiment (Sun *et al.* 2006). In that experiment, the space-resolved PIV data were used to calculate the longitudinal velocity SFs. The two sets of data superimpose with each other and are well described by (3.8) (solid line). Owing to the limited statistics of the velocity data, we are only able to obtain the scaling exponent $\gamma_\tau^u(n)$ reliably up to $n = 4$.

Figure 12(*b*) shows the reduced exponent $\zeta_u(n)/\zeta_u(2)$ at the cell centre (circles, red online). For comparison, the space-resolved PIV data by Sun *et al.* (2006) (triangles, black) are also included. It is seen that the two sets of data obtained from different experiments and by different methods agree well within the experimental uncertainties. Similar to the situation near the sidewall, the use of the reduced exponent $\zeta_u(n)/\zeta_u(2)$ helps to reduce systematic errors in the experiment. The value of $\zeta_u(2)$ was found to vary from 0.68 at the cell centre to 0.78 near the sidewall (Sun *et al.* 2006). Because the velocity sampling rate at the cell centre was even lower than that near the sidewall, we are only able to obtain $\gamma_\tau^u(n)$ reliably up to $n = 2.5$. The measured $\zeta_u(n)/\zeta_u(2)$ at the cell centre can also be well described by (3.8) (solid line). Figure 12 thus suggests that the most dissipative structures of the velocity field in turbulent RBC remain the same across the convection cell and they are filament-like ($c_u = 2$).

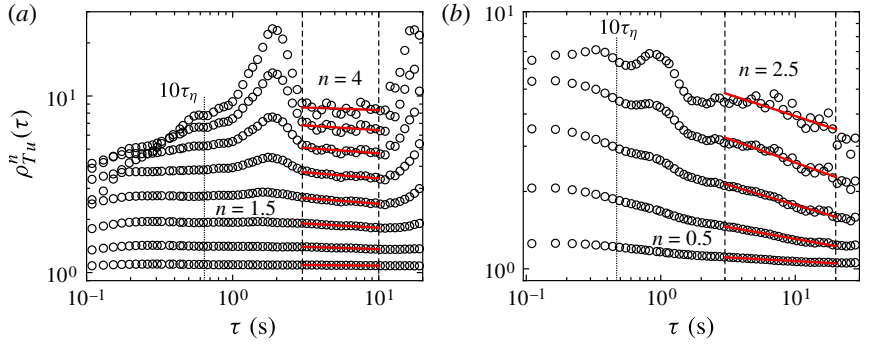

FIGURE 13. (Colour online) (*a*) Measured correlation function $\rho^n_{Tu}(\tau)$ versus delay time τ near the sidewall at $Ra = 9.5 \times 10^9$. From the bottom to the top, the values of n is increased from $n = 0.5$ to $n = 4$ with an increment of 0.5. (*b*) Measured $\rho^n_{Tu}(\tau)$ as a function of τ at the cell centre with $Ra = 1.4 \times 10^{10}$. From the bottom to the top, the values of n is increased from $n = 0.5$ to $n = 2.5$ with an increment of 0.5. In (*a*) and (*b*), the solid lines (red online) show the power-law fits to the data in a common scaling range in τ as marked by the two vertical dashed lines. The dotted lines represent $10\tau_\eta$ calculated for the two values of *Ra*.

We now discuss the correlation function $\rho^n_{Tu}(\tau)$ between the velocity moments δu^n_τ and temperature moments δT^{2n}_τ, which is defined as

$$\rho^n_{Tu}(\tau) \equiv \frac{\langle \delta u^n(\tau)\delta T^{2n}(\tau)\rangle}{\langle \delta u^n(\tau)\rangle\langle \delta T^{2n}(\tau)\rangle} \sim \tau^{\phi(n,2n)}. \tag{C 1}$$

Figure 13(*a*) shows the measured correlation function $\rho^n_{Tu}(\tau)$ near the sidewall at $Ra = 9.5 \times 10^9$ for different values of n from 0.5 to 4 with an increment of 0.5 (bottom to top). In the plot, the dotted line represents $10\tau_\eta$ with the dissipation time $\tau_\eta \simeq 6.4 \times 10^{-2}$ s associated with the Komogorov length η (see appendix A). In a common range of τ as marked by the two vertical dashed lines in figure 13(*a*), the measured $\rho^n_{Tu}(\tau)$ reveals a good power-law scaling for all values of n up to 4 (solid lines, red online). The scaling range in τ is slightly over a half-decade long between $47\tau_\eta$ and $157\tau_\eta$. For the common scaling region in τ, we use the least-squares method to fit all the data and obtain $\phi(n, 2n)$ for different values of n up to 4. In the calculation of $\rho^n_{Tu}(\tau)$ near the sidewall, 5×10^6 data points are used to ensure that the resulting $\phi(n, 2n)$ is accurate up to $n = 4$. The obtained values of $\phi(n, 2n)$ are given in table 1. It is found that the τ-dependence of the measured $\rho^n_{Tu}(\tau)$ is weak and the obtained values of $\phi(n, 2n)$ are very small (close to zero) for all values of n up to 4. Figure 13(*a*) thus suggests that the correlation between the velocity moments δu^n_τ and temperature moments δT^{2n}_τ is very weak near the sidewall.

Figure 13(*b*) shows the measured $\rho^n_{Tu}(\tau)$ as a function of τ at the cell centre for different values of n from 0.5 to 2.5 with an increment of 0.5 (bottom to top). In the plot, the dotted line represents $10\tau_\eta$ with $\tau_\eta \simeq 4.7 \times 10^{-2}$ s at $Ra = 1.4 \times 10^{10}$. Similar to the situation near the sidewall, the measured $\rho^n_{Tu}(\tau)$ reveals a good power-law scaling (solid lines, red online) in a common range of τ as marked by the two vertical dashed lines in figure 13(*b*). The scaling range in τ is close to a decade long between $64\tau_\eta$ and $425\tau_\eta$. Owing to the low-velocity sampling rate at the cell centre, there were only $\sim 10^6$ data points available. Thus, we are only able to obtain $\phi(n, 2n)$

accurately up to $n = 2.5$. The obtained values of $\phi(n, 2n)$ are given in table 1. It is seen that the τ-dependence of the measured $\rho^n_{Tu}(\tau)$ at the cell centre is much stronger than that near the sidewall and this correlation increases with n. Figure 13(*b*) thus suggests that the correlation between the velocity moments δu^n_τ and temperature moments δT^{2n}_τ is stronger at the cell centre and increases with the order n of the moments.

REFERENCES

ANTONIA, R. A., HOPFINGER, E. J., GAGNE, Y. & ANSELMET, F. 1984 Temperature structure functions in turbulent shear flows. *Phys. Rev.* A **30**, 2704–2707.

ARNÈODO, A., BENZI, R., BERG, J., BIFERALE, L., BODENSCHATZ, E., BUSSE, A., CALZAVARINI, E., CASTAING, B., CENCINI, M., CHEVILLARD, L., FISHER, R. T., GRAUER, R., HOMANN, H., LAMB, D., LANOTTE, A. S., LÉVÉQUE, E., LÜTHI, B., MANN, J., MORDANT, N., MÜLLER, W.-C., OTT, S., OUELLETTE, N. T., PINTON, J.-F., POPE, S. B., ROUX, S. G., TOSCHI, F., XU, H. & YEUNG, P. K. 2008 Universal intermittent properties of particle trajectories in highly turbulent flows. *Phys. Rev. Lett.* **100**, 254504.

ASHKENAZI, S. & STEINBERG, V. 1999 Spectra and statistics of velocity and temperature fluctuations in turbulent convection. *Phys. Rev. Lett.* **83**, 4760–4763.

BELMONTE, A. & LIBCHABER, A. 1996 Thermal signature of plumes in turbulent convection: the skewness of the derivative. *Phys. Rev.* E **53**, 4893–4898.

BENZI, R., CILIBERTO, S., TRIPICCIONE, R., BAUDET, C., MASSAIOLI, F. & SUCCI, S. 1993 Extended self-similarity in turbulent flows. *Phys. Rev.* E **48**, R29–R32.

BENZI, R., TOSCHI, F. & TRIPICCIONE, R. 1998 On the heat transfer in Rayleigh–Bénard systems. *J. Stat. Phys.* **93**, 901–918.

BENZI, R., TRIPICCIONE, R., MASSAIOLI, F., SUCCI, S. & CILIBERTOI, S. 1994 On the scaling of the velocity and temperature structure functions in Rayleigh–Bénard convection. *Europhys. Lett.* **25**, 341–346.

BIFERALE, L. & PROCACCIA, I. 2005 Anisotropy in turbulent flows and in turbulent transport. *Phys. Rep.* **414**, 43–164.

BORATAV, O. N. & PELZ, R. B. 1998 Coupling between anomalous velocity and passive scalar increments in turbulence. *Phys. Fluids* **10**, 2122–2124.

CALZAVARINI, E., TOSCHI, F. & TRIPICCIONE, R. 2002 Evidences of Bolgiano–Obhukhov scaling in three-dimensional Rayleigh–Bénard convection. *Phys. Rev.* E **66**, 016304.

CAMUSSI, R. & VERZICCO, R. 2004 Temporal statistics in high Rayleigh number convective turbulence. *Eur. J. Mech. (*B*/Fluids)* **23**, 427–442.

CAO, N. & CHEN, S. 1997 An intermittency model for passive-scalar turbulence. *Phys. Fluids* **9**, 1203–1205.

CAO, N., CHEN, S. & SREENIVASAN, K. R. 1996 Scalings of low-order structure functions in fluid turbulence. *Phys. Rev. Lett.* **77**, 3799–3802.

CHAVANNE, X., CHILLÀ, F., CHABAUD, B., CASTAING, B. & HÉBRAL, B. 2001 Turbulent Rayleigh–Bénard convection in gaseous and liquid He. *Phys. Fluids* **13**, 1300–1320.

CHEN, S., SREENIVASAN, K. R., NELKIN, M. & CAO, N.-Z. 1997 Refined similarity hypothesis for transverse structure functions in fluid turbulence. *Phys. Rev. Lett.* **79**, 2253–2256.

CHERTKOV, M., FALKOVICH, G., KOLOKOLOV, I. & LEBEDEV, V. 1995 Normal and anomalous scaling of 4He fourth-order correlation function of a randomly advected passive scalar. *Phys. Rev.* E **52**, 4924–4941.

CHILLA, F. & SCHUMACHER, J. 2012 New perspectives in turbulent Rayleigh–Bénard convection. *Eur. Phys. J.* E **35**, 58.

CHING, E. S. C., LEUNG, C. K., QIU, X.-L. & TONG, P. 2003 Intermittency of velocity fluctuations in turbulent thermal convection. *Phys. Rev.* E **68**, 026307.

CHING, E. S. C. 2007 Measured thermal dissipation field in turbulent Rayleigh–Bénard convection. *Phys. Rev.* E **75**, 056302.

CHING, E. S. C. & CHAU, K. L. 2001 Scaling laws in the central region of confined turbulent thermal convection. *Phys. Rev.* E **63**, 047303.

CHING, E. S. C., GUO, H. & LO, T. S. 2008 Refined similarity hypotheses in shell models of homogeneous turbulence and turbulent convection. *Phys. Rev.* E **78**, 026303.

CHING, E. S. C. & KWOK, C. Y. 2000 Statistics of local temperature dissipation in high Rayleigh number convection. *Phys. Rev.* E **62**, R7587–R7590.

CIONI, S., CILIBERTO, S. & SOMMERIA, J. 1995 Temperature structure functions in turbulent convection at low Prandtl number. *Europhys. Lett.* **32**, 413–418.

CORRSIN, S. 1951 On the spectrum of isotropic temperature fluctuations in an isotropic turbulence. *J. Appl. Phys.* **22**, 469–473.

DU, Y.-B. & TONG, P. 2000 Turbulent thermal convection in a cell with ordered rough boundaries. *J. Fluid Mech.* **407**, 57–84.

FALKOVICH, G., GAWEDZKI, K. & VERGASSOLA, M. 2001 Particles and fields in fluid turbulence. *Rev. Mod. Phys.* **73**, 913–975.

FRISCH, U. 1995 *Turbulence: the Legacy of A. N. Kolmogorov*. Cambridge University Press.

FRISCH, U., MAZZINO, A. & VERGASSOLA, M. 1998 Intermittency in passive scalar advection. *Phys. Rev. Lett.* **80**, 5532–5535.

GAWĘDZKI, K. & KUPIAINEN, A. 1995 Anomalous scaling of the passive scalar. *Phys. Rev. Lett.* **75**, 3834.

GROSSMANN, S. & LOHSE, D. 1992 Scaling in hard turbulent Rayleigh–Bénard flow. *Phys. Rev.* A **46**, 903–917.

GROSSMANN, S. & LOHSE, D. 1993 Characteristic scales in Rayleigh–Bénard turbulence. *Phys. Lett.* A **173**, 58–62.

GROSSMANN, S., LOHSE, D. & REEH, A. 1997 Different intermittency for longitudinal and transversal turbulent fluctuations. *Phys. Fluids* **9**, 3817–3825.

GYLFASON, A. & WARHAFT, Z. 2004 On higher order passive scalar structure functions in grid turbulence. *Phys. Fluids* **16**, 4012–4019.

HE, G.-W., CHEN, S. & DOOLEN, G. 1998 Hierarchy of structure functions for passive scalars advected by turbulent flows. *Phys. Lett.* A **246**, 135–138.

HE, G.-W. & ZHANG, J.-B. 2006 Elliptic model for space–time correlations in turbulent shear flows. *Phys. Rev.* E **73**, 055303(R).

HE, X., CHING, E. S. C. & TONG, P. 2011 Locally averaged thermal dissipation rate in turbulent thermal convection: a decomposition into contributions from different temperature gradient components. *Phys. Fluids* **23**, 025106.

HE, X., FUNFSCHILLING, D., NOBACH, H., BODENSCHATZ, E. & AHLERS, G. 2012 Transition to the ultimate state of turbulent Rayleigh–Bénard convection. *Phys. Rev. Lett.* **108**, 024502.

HE, X., HE, G. & TONG, P. 2010*a* Small-scale turbulent fluctuations beyond Taylor's frozen-flow hypothesis. *Phys. Rev.* E **81**, 065303(R).

HE, X. & TONG, P. 2009 Measurements of the thermal dissipation field in turbulent Rayleigh–Bénard convection. *Phys. Rev.* E **79**, 026306.

HE, X. & TONG, P. 2011 Kraichnan's random sweeping hypothesis in homogeneous turbulent convection. *Phys. Rev.* E **83**, 037302.

HE, X., TONG, P. & CHING, E. S. C. 2010*b* Statistics of the locally averaged thermal dissipation rate in turbulent Rayleigh–Bénard convection. *J. Turbul.* **11**, 1–10.

HE, X., TONG, P. & XIA, K.-Q. 2007 Measured thermal dissipation field in turbulent Rayleigh–Bénard convection. *Phys. Rev. Lett.* **98**, 144501.

ISHIHARA, T., GOTOH, T. & KANEDA, Y. 2009 Study of high-Reynolds number isotropic turbulence by direct numerical simulation. *Annu. Rev. Fluid Mech.* **41**, 165–180.

KADANOFF, L. P. 2001 Turbulent heat flow: structures and scaling. *Phys. Today* **54**, 34–39.

KERR, R. 1996 Rayleigh number scaling in numerical convection. *J. Fluid Mech.* **310**, 139–179.

KOLMOGOROV, A. N. 1941 The local structure of turbulence in incompressible viscous fluid for very large Reynolds numbers. *Dokl. Akad. Nauk SSSR* **30**, 301–305.

KOLMOGOROV, A. N. 1962 A refinement of previous hypotheses concerning the local structure of turbulence in a viscous incompressible fluid at high Reynolds number. *J. Fluid Mech.* **13**, 82–85.

KRAICHNAN, R. H. 1964 Kolmogorov's hypotheses and Eulerian turbulence theory. *Phys. Fluids* **7**, 1723–1734.

KRAICHNAN, R. H. 1974 Convection of a passive scalar by a quasi-uniform random stretching field. *J. Fluid Mech.* **64**, 737–762.

KRAICHNAN, R. H. 1994 Anomalous scaling of a randomly advected passive scalar. *Phys. Rev. Lett.* **72**, 1016–1019.

KUNNEN, R. P. J., CLERCX, H. J. H., GEURTS, B. J., VAN BOKHOVEN, L. J. A., AKKERMANS, R. A. D. & VERZICCO, R. 2008 Numerical and experimental investigation of structure-function scaling in turbulent Rayleigh–Bénard convection. *Phys. Rev.* E **77**, 016302.

LASHERMES, B., ABRY, P. & CHAINAIS, P. 2004 New insights into the estimation of scaling exponents. *Intl J. Wavelets Multiresolut. Inf. Process.* **2**, 497–530.

LEPORE, J. & MYDLARSKI, L. 2009 Effect of the scalar injection mechanism on passive scalar structure functions in a turbulent flow. *Phys. Rev. Lett.* **103**, 034501.

LOHSE, D. & XIA, K.-Q. 2010 Small-scale properties of turbulent Rayleigh–Bénard convection. *Annu. Rev. Fluid Mech.* **42**, 335–364.

MASHIKO, T., TSUJI, Y., MIZUNO, T. & SANO, M. 2004 Instantaneous measurement of velocity fields in developed thermal turbulence in mercury. *Phys. Rev.* E **69**, 036306.

MENEVEAU, C., SREENIVASAN, K. R., KAILASNATH, P. & FAN, M. S. 1990 Joint multifractal measures: theory and applications to turbulence. *Phys. Rev.* A **41**, 894–913.

OBUKHOV, A. M. 1949 Structure of the temperature field in turbulent flow. *Izv. Akad. Nauk SSSR Geogr. Geofiz* **13**, 58–69.

PROCACCIA, I., CHING, E. S. C., CONSTANTIN, P., KADANOFF, L. P., LIBCHABER, A. & WU, X.-Z. 1991 Transitions in convective turbulence: the role of thermal plumes. *Phys. Rev.* A **44**, 8091–8102.

PROCACCIA, I. & ZEITAK, R. 1989 Scaling exponents in nonisotropic convective turbulence. *Phys. Rev. Lett.* **62**, 2128–2131.

PROCACCIA, I. & ZEITAK, R. 1990 Scaling exponents in thermally driven turbulence. *Phys. Rev.* A **42**, 821–830.

QIU, X.-L. & TONG, P. 2001 Large-scale velocity structures in turbulent thermal convection. *Phys. Rev.* E **64**, 036304.

QIU, X.-L. & TONG, P. 2002 Temperature oscilations in turbulent Rayleigh–Bénard convection. *Phys. Rev.* E **66**, 026308.

RUIZ-CHAVARRIA, G., BAUDET, C. & CILIBERTO, S. 1996 Scaling laws and dissipation scale of a passive scalar in fully developed turbulence. *Physica* D **99**, 369–380.

SADDOUGHI, S. G. & VEERAVALLI, S. V. 1994 Local isotropy in turbulent boundary layers at high Reynolds number. *J. Fluid Mech.* **268**, 333–372.

SHANG, X.-D., TONG, P. & XIA, K.-Q. 2008 Scaling of the local convective heat flux in turbulent Rayleigh–Bénard convection. *Phys. Rev. Lett.* **100**, 244503.

SHANG, X.-D., QIU, X. L., TONG, P. & XIA, K. Q. 2003 Measured local heat transport in turbulent Rayleigh–Bénard convection. *Phys. Rev. Lett.* **90**, 074501.

SHANG, X.-D., QIU, X.-L., TONG, P. & XIA, K.-Q. 2004 Measurements of the local convective heat flux in turbulent Rayleigh–Bénard convection. *Phys. Rev.* E **70**, 026308.

SHE, Z.-S. & LÉVEQUE, E. 1994 Universal scaling laws in fully developed turbulence. *Phys. Rev. Lett.* **72**, 336–339.

SHE, Z.-S. & ORSZAG, S. A. 1991 Physical model of intermittency: inertial-range non-Gaussian statistics. *Phys. Rev. Lett.* **66**, 1701–1704.

SHRAIMAN, B. & SIGGIA, E. 1995 Anomalous scaling of a passive scalar in turbulent fow. *C. R. Acad. Sci.* **321**, 279–284.

SHRAIMAN, B. I. & SIGGIA, E. D. 2000 Scalar turbulence. *Nature* **405**, 639–646.

SIGGIA, E. D. 1994 High Rayleigh number convection. *Annu. Rev. Fluid Mech.* **26**, 137–168.

SKRBEK, L., NIEMELA, J. J., SREENIVASAN, K. R. & DONNELLY, R. J. 2002 Temperature structure functions in the Bolgiano regime of thermal convection. *Phys. Rev.* E **66**, 036303.

SREENIVASAN, K. R. 1991*a* Fractals and multifractals in fluid turbulence. *Annu. Rev. Fluid Mech.* **233**, 539–600.

SREENIVASAN, K. R. 1991*b* On local isotropy of passive scalars in turbulent shear flows. *Proc. R. Soc. Lond.* A **434**, 165–182.

SUN, C., XIA, K.-Q. & TONG, P. 2005 Three-dimensional flow structures and dynamics of turbulent thermal convection in a cylindrical cell. *Phys. Rev.* E **72**, 026302.

SUN, C., ZHOU, Q. & XIA, K.-Q. 2006 Cascades of velocity and temperature fluctuations in buoyancy-driven thermal turbulence. *Phys. Rev. Lett.* **97**, 144504.

TAKESHITA, T., SEGAWA, T., GLAZIER, J. A. & SANO, M. 1996 Thermal turbulence in mercury. *Phys. Rev. Lett.* **76**, 1465–1468.

TAYLOR, G. I. 1938 The spectrum of turbulence. *Proc. R. Soc. Lond.* A **164**, 476–490.

TONG, P. & SHEN, Y. 1992 Relative velocity fluctuations in turbulent Rayleigh–Bénard convection. *Phys. Rev. Lett.* **69**, 2066–2069.

WARHAFT, Z. 2000 Passive scalars in turbulent flows. *Annu. Rev. Fluid Mech.* **32**, 203–240.

WU, X.-Z., KADANOFF, L. P., LIBCHABER, A. & SANO, M. 1990 Frequency power spectrum of temperature fluctuations in free convection. *Phys. Rev. Lett.* **64**, 2140.

XI, H.-D., LAM, S. & XIA, K.-Q. 2004 From laminar plumes to organized flows: the onset of large-scale circulation. *J. Fluid Mech.* **503**, 47–56.

XI, H.-D. & XIA, K.-Q. 2008 Azimuthal motion, reorientation, cessation, and reversal of the large-scale circulation in turbulent thermal convection: a comparative study in aspect ratio one and one-half geometries. *Phys. Rev.* E **78**, 036326.

YAGLOM, A. M. 1949 On the local structure of the temperature field in a turbulent flow. *Dokl. Akad. Nauk SSSR* **69**, 743–746.

ZHAO, X. & HE, G. W. 2009 Space–time correlations of fluctuating velocities in turbulent shear flows. *Phys. Rev.* E **79**, 046316.

ZHOU, Q., LI, C.-M., LU, Z.-M. & LIU, Y.-L. 2011 Experimental investigation of longitudinal space–time correlations of the velocity field in turbulent Rayleigh–Bénard convection. *J. Fluid Mech.* **683**, 94–111.

ZHOU, Q., SUN, C. & XIA, K.-Q. 2008 Experimental investigation of homogeneity, isotropy, and circulation of the velocity field in buoyancy-driven turbulence. *J. Fluid Mech.* **598**, 361–372.

ZHOU, S.-Q. & XIA, K.-Q. 2001 Scaling properties of the temperature field in convective turbulence. *Phys. Rev. Lett.* **87**, 064501.